ACS Catalysis

Editors' Choice

Open Access

pubs.acs.org/acscatalysis

Research Article

Role of Defects in Reversible Surface Restructuring and Activity of Co_3O_4 Oxygen Evolution Electrocatalysts

Carl Hendric Scharf, Alex Chandraraj, Konrad Dyk, Felix Stebner, Sören Lepin, Jing Tian, Laila El Bergmi Byaz, Jochim Stettner, Christian Leppin, Anastasiia Kotova, Sebastian Reinke, Julia Linnemann,* Fouad Maroun,* and Olaf M. Magnussen*

Cite This: *ACS Catal.* 2026, 16, 4877−4891

Read Online

ACCESS | Metrics & More | Article Recommendations | Supporting Information

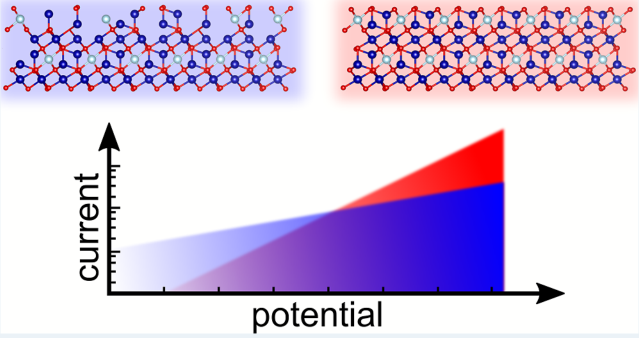

ABSTRACT: Overcoming the slow kinetics of the oxygen evolution reaction at the anode is a key challenge for the production of hydrogen via electrolysis. This reaction operates at very positive potentials, where the electrocatalyst is exposed to highly oxidative conditions and prone to potential-dependent transformation of the near-surface region. While substantial evidence for such surface restructuring exists, its extent and relevance for the catalyst's activity are unclear. We address this topic for the case of Co_3O_4, one of the best-known electrocatalysts exhibiting surface restructuring, by studies of epitaxial (111)-ordered electrodeposited films with combined *operando* X-ray surface diffraction and absorption spectroscopy, electrochemical impedance spectroscopy, and electrochemical measurements on rotating disk electrodes. Comparison of the as-prepared and annealed state of the same samples, which both are stable even under long-term oxygen evolution conditions, provides clear insight into the role of surface defects. Our results show that defect-free annealed $Co_3O_4(111)$ surfaces are structurally stable over a wide potential range and hydroxylate via adsorption at surface oxygen and Co sites. Potential-induced surface restructuring of the Co_3O_4 lattice occurs only in the presence of surface defects, leading to the formation of the well-known nanometer-thick oxyhydroxide skin layer. The presence of this skin layer promotes oxygen evolution at low overpotentials but results in higher Tafel slopes. As a result, highly ordered $Co_3O_4(111)$ surfaces are more active at high current densities than defective Co_3O_4 surfaces that undergo surface restructuring. These results highlight that strategies for catalyst surface defect engineering need to be application-oriented.

KEYWORDS: *electrocatalysis, oxygen evolution, Co oxide, operando studies, X-ray diffraction, impedance spectroscopy*

INTRODUCTION

The need for efficient technologies for sustainable energy conversion has driven extensive research on electrochemical and photoelectrochemical water splitting.[1] Here, anodes for the oxygen evolution reaction (OER) have been identified as a key bottleneck due to the sluggish kinetics of this electrocatalytic reaction. In alkaline to neutral electrolyte, the arguably most important OER catalysts are transition-metal oxides, especially of cobalt, iron, and nickel, which are highly efficient, stable, and abundant.[2−6] In particular, cobalt-based materials have been studied extensively by experimental methods[4−24] as well as *ab initio* theory,[21,25−32] aiming to understand the microscopic processes of the OER at oxide-electrolyte interfaces and by this enable a knowledge-based development of improved electrocatalysts.

It is nowadays well-known that many electrocatalyst materials are not perfectly stable but transform under reaction conditions within a near-surface region.[33,34] The restructuring of the catalyst may be irreversible or highly reversible and induced by the presence of the electrolyte, the applied potential, or the reaction itself. OER catalysts are particularly prone to surface restructuring, owing to the highly oxidative conditions during anodic oxygen evolution. The relevance of such structural transformations for the catalytic properties is a topic of strong current debate. It has been proposed that lability with respect to structural transformations is of essential relevance for the catalyst's activity.[35,36] Cobalt (hydr)oxide electrocatalysts are a prime example of such effects. *Operando* studies have revealed potential-dependent surface phase transformations on $Co(OH)_2$,[18] on (hydrated) CoOOH,[19]

Received: December 10, 2025
Revised: January 23, 2026
Accepted: January 30, 2026
Published: February 16, 2026

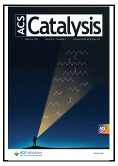

https://doi.org/10.1021/acscatal.5c08785

and, especially, on Co_3O_4 where highly reversible restructuring of the spinel lattice in a near-surface region was observed by potential-dependent X-ray diffraction and spectroscopic measurements.[7,9−13]

Studies of epitaxial Co_3O_4(111) thin film model catalysts, prepared by electrodeposition, showed this structural transformation to start at potentials several hundred millivolts negative of the onset of the OER.[10] The thickness of the transformed region, termed the skin layer, changed with potential and ranged from ≤0.2 to 4 nm, depending on the preparation conditions and morphology of the epitaxial film.[11] Correlative surface X-ray diffraction (SXRD) and X-ray absorption spectroscopy (XAS) studies indicated that the Co-oxidation state in the skin layer is 3+, suggesting a CoOOH phase.[12] Co_3O_4(111) films prepared by different procedures exhibited a pronounced increase in OER activity with increasing average thickness of the formed skin layer.[11] Based on these results, it was suggested that the entire skin layer is a three-dimensional reaction zone for the OER. Specifically, it was found that samples prepared by pulsed vapor deposition (PVD) and annealing under ultrahigh vacuum (UHV) conditions remained almost skin layer free, i.e., showed only negligible potential-dependent structural transformations. The latter samples were found to exhibit considerably higher OER overpotentials, which was also confirmed in other studies of PVD-prepared Co_3O_4(111) films.[16,17] Interestingly, electrodeposited epitaxial CoOOH(0001) films exhibited a similar OER activity as the most active Co_3O_4(111) films, although no surface restructuring and only minor changes in Co-oxidation state were observed.[10,12] The latter was attributed to potential-induced surface hydroxylation. Indications for (irreversible) hydroxylation of epitaxial Co_3O_4 model catalysts were also found for PVD-prepared films transferred under an oxygen-free atmosphere between UHV and electrochemical environment.[14−17] In addition, these *ex situ* studies also indicated a larger thickness of the hydroxyl layer and higher OER activity for (100)-oriented as compared to (111)-oriented Co_3O_4 films.[17] These changes were interpreted in terms of a different amount of skin layer formation. Whether the latter assignment is correct is unclear, however, as the surface structure was not determined *in operando* in these studies.

All these model catalyst studies provide strong evidence that the preparation conditions and the resulting sample morphology and surface defect structure have a pronounced influence on the tendency of Co oxide electrode surfaces toward restructuring and on the electrochemical properties. These effects can be substantial and even exceed those of the surface orientation and chemical nature of the Co oxide. For example, the OER overpotentials at 1 mA/cm^2 of differently prepared Co_3O_4(111) films varied by as much as 120 mV,[11] despite identical bulk structure and surface orientation. In contrast, the corresponding overpotentials of PVD-prepared Co_3O_4(111) and Co_3O_4(100) films differed by only 30 mV[17] and those of electrodeposited Co_3O_4(111) and CoOOH(0001) films by just 10 mV. Understanding of these effects is urgently necessary to apply the insights obtained on model catalysts to real oxide electrocatalysts and employ them for surface and defect engineering of these materials.

In this work, we directly tune the surface defect structure of Co_3O_4(111) model catalysts and investigate its effect on the lability toward potential-induced surface transformations and OER activity. We show that surface defects can be efficiently removed by thermal annealing, with drastic effects on the behavior observed in correlative structural and electrochemical studies. In particular, we address these topics with a novel combination of *operando* SXRD and electrochemical impedance spectroscopy (EIS) measurements, which allows the catalyst's (near-)surface structure to be linked with its detailed electrochemical response. This correlative multimethod approach allows detailed EIS characterization of samples with a well-known amount of skin layer formation. Furthermore, we also perform electrochemical studies of these epitaxial model catalysts under well-controlled hydrodynamic conditions, provide data on the oxidation state changes by combined *in situ* SXRD and XAS measurements, and characterize the film morphology and crystal structure by AFM and XRD. Together, these studies allow a comprehensive comparison of the structural behavior before and after annealing and show unambiguously the influence of defects on the electrochemical behavior. According to these comprehensive measurements, thermal annealing can significantly affect the structural transformation of the Co_3O_4 surface and can completely suppress reversible skin layer formation, allowing assessment of the skin layer's effect on the individual subprocesses of the OER identified by EIS as well as on the pseudocapacitive behavior in the pre-OER potential region. The as-prepared transformation labile surface structure and the annealed structurally stable surface of the Co_3O_4 electrode are both remarkably long-lasting and OER active. We discuss the microscopic origin of these effects and their relevance for understanding the OER mechanisms on Co oxide electrocatalysts and their modification by surface engineering.

■ EXPERIMENTAL SECTION

Sample Preparation and Characterization

The sample preparation procedure was adapted from ref 37 and is described in detail in refs 10, 11 and 38. Thin epitaxial cobalt oxide films were electrodeposited on hat-shaped Au(111) single crystals (MaTeck) with a surface diameter of 4 mm and an orientation uncertainty of ≤0.1°. Prior to oxide film preparation, the Au crystal was immersed in a hot 1:2 mixture of 30% H_2O_2 and 96% H_2SO_4 (both Carl Roth, ROTIPURAN, p.a., ISO) for 1 min to remove any remaining oxide from previous experiments and then annealed in a butane flame for 5 min. To deposit the Co oxide film, the Au crystal was immersed in an aqueous, oxygen-free solution of 1 mM $Co(NO_3)_2$ + 1.2 mM L-(+)-tartaric acid + 1 M NaOH, prepared from high-purity Co(II) nitrate hexahydrate (Sigma-Aldrich, EMSURE, ≥99.0%), L-(+)-tartaric acid (Sigma-Aldrich, ACS reagent grade, ≥99.5%), NaOH (Sigma-Aldrich, EMPLURA, ≥97%, Fe content ≤ 0.002%), and Milli-Q water. The electrodeposition was performed at ∼95 °C at a constant potential of −0.151 V vs a saturated calomel reference electrode (i.e., 0.916 V vs the reversible hydrogen electrode), where the Co(II) complex is oxidized and Co(III) precipitates on the electrode surface. A charge density of 8 mC/cm^2 was passed to grow Co_3O_4 films with (111) orientation of ∼30−60 nm thickness (thickness variation resulting from exposure of the rough, spark-eroded mantle surface of the cylindrical Au crystal to the electrolyte, which differs in electrochemical surface area for the different employed Au crystals). CoOOH films were prepared in an identical way by electrodeposition from a 5 M NaOH base electrolyte. After deposition, the samples were quickly removed from the deposition cell, rinsed with ultrapure water, dried with Ar, and stored in air until the measurements. The morphology of the samples was characterized under ambient conditions with atomic force microscopy (Bruker Dimension 3100) using the tapping mode. Aluminum reflex-coated silicon AFM tips with a cantilever oscillating frequency of 150 or 300 kHz (BudgetSensors) were used (both having a tip radius of

10 nm and a half cone angle of 20−25° along the cantilever axis, 25−30° from the side, and 10° at the apex). Different regions of the sample were imaged to ensure that the observed morphology was representative of the sample morphology.

Electrochemical Characterization

Electrochemical characterization of the Co oxide catalysts was performed both in the electrochemical cell used in the *operando* SXRD studies and employed in our previous work[10] as well as in a new dedicated setup, employing a rotating disk electrode (RDE). The RDE setup consists of a commercial rotator (Pine Research Instrumentation) and a glass cell containing ∼180 mL of electrolyte. The Pt wire serving as the counter electrode and the Hg/HgO (0.1 M KOH) reference electrode were placed directly in the glass cell. The samples are embedded in a Teflon holder with a flat top surface, which exposes only the (111)-oriented top part of the Au single crystal sample with the epitaxial Co oxide film to be studied. Rotation rates of 1600 and 3000 rpm were used, providing almost identical electrochemical data. All electrochemical experiments within this work were performed in 0.1 M NaOH electrolyte (Sigma-Aldrich, EMPLURA) that had been degassed with Ar (5.0) for at least 20 min. During the experiments, the cells were continuously purged with Ar to maintain an inert atmosphere. Additional electrochemical studies and *operando* SXRD studies were performed in the cell used in our previous work, which contains an electrolyte volume of ∼2 mL.[10] In this cell, the samples are sealed with a Teflon cone, which exposes only the top part of the sample to the electrolyte. Potential control was established using a Pt wire as a counter electrode and a Ag/AgCl (3.4 M KCl) micro reference electrode via a glass capillary. The reference electrode was equipped with a 10 nF bypass capacitor connected to Pt wire to reduce the high-frequency artifacts. The electrolyte was continuously exchanged via a remote-controlled pumping system at an exchange rate of 5 μL/s. For measurements in both cells, a Biologic SP-200 or SP-300 potentiostat was used. All potentials within this work are *iR*-corrected and are given throughout the text with respect to the reversible hydrogen electrode (RHE) to ease comparison with the literature. *iR*-correction in the RDE cell was performed by hardware compensation of the potentiostat. Data obtained in the SXRD cell were *iR*-corrected manually after the measurements. Small potential shifts of the reference electrode in the SXRD cell (below 40 mV) were corrected by comparing the capacitive region of the CVs to that of the highly reproducible CVs recorded in the RDE cell. Current densities were calculated with respect to the geometric surface area of the crystal (0.125 cm^2). These corrections were applied for all potentiodynamic measurements, including *operando* SXRD experiments.

Surface X-ray Diffraction

Operando SXRD studies were conducted at PETRA III beamline *P*23 of DESY at a photon energy of 22.5 keV, a photon flux of ∼6×10^{10} counts/s, and a beam size of 300 μm (h) × 70 μm (v), employing the same approach as in our previous studies.[10,11,13] All measurements were performed on the Eulerian cradle in a six-circle geometry at a fixed grazing incidence angle of 1°, resulting in a footprint of the beam on the sample of 300 μm × 4 mm. The X-ray diffraction signal was monitored by a 2D LAMBDA 250 k GaAs detector. The combined *operando* SXRD/EIS measurements were performed in the SXRD cell using a Solartron ModuLab XM ECS potentiostat. The electrochemical current as well as the optical reflectivity (measured with a 630 nm laser diode at normal incidence) were recorded simultaneously with the X-ray detector images. Structural properties of the Co oxide film were obtained by continuously monitoring a single Bragg peak position ($Co_3O_4(1\bar{1}3)$ or CoOOH(017)) at a rate of 1 s^{-1} during potential cycling at 5 mV/s (recording 2 cycles in each experiment). To ease comparison with the literature, the Bragg peaks of the studied Co_3O_4 and CoOOH films refer to the conventional simple cubic and hexagonal unit cells of these materials, respectively. To extract structural properties (strain and grain size) of the Co oxide film as a function of the applied electrode potential, the intensity distribution at the corresponding Bragg peak of each 2D detector frame was first converted to the reciprocal space. Subsequently, one-dimensional projections of the peak intensity in horizontal and vertical directions were fitted with a Pseudo-Voigt function. The peak positions $q_{\perp,\parallel}$ and the full widths at half-maximum $\mathrm{fwhm}_{\perp,\parallel}$ allow the determination of the lattice strain $\varepsilon_{\perp,\parallel} = \frac{q_{\perp,\parallel,\mathrm{nom}}}{q_{\perp,\parallel}} - 1$ and the coherence length $d_{\perp,\parallel} = \frac{2\pi}{\mathrm{FWHM}_{\perp,\parallel}}$, which is associated with the crystallite size (∥ and ⊥ corresponding to the surface in-plane and out-of-plane directions, respectively).

Combined Surface X-ray Diffraction and X-ray Absorption Spectroscopy

Combined *in situ* SXRD and X-ray absorption near-edge spectroscopy (XANES) measurements were performed at the DiffAbs beamline of Soleil Synchrotron (Saint-Aubin, France), employing identical methods, as described in detail in ref 12. Briefly, the Co_3O_4 thin film sample was measured at an incident beam angle of 4° in a thin layer electrochemical cell with a 12 μm thick polypropylene membrane. The XRD data was collected using a XPAD S140 2D detector. The intensity of X-ray fluorescence was recorded using a 4-element SDD detector placed at 90° from the incident beam at the height of the sample surface. The spectral resolution of the detector allows separation of the Co fluorescence from other contributions. To perform the simultaneous XRD and XAS measurements, we first acquired a XANES spectrum to determine the Co edge energy and the change of the Co fluorescence intensity with photon energy at the Co edge ($dI_{\mathrm{Co}}/dE_{\mathrm{Ph}}$). Then, the incident beam energy was fixed at the Co edge energy, and the sample and the XRD detector were positioned to collect the Co($1\bar{1}3$) diffraction peak. From the XPAD images and Co fluorescence, recorded as a function of potential during CVs at 5 mV/s, the skin layer thickness and edge energy change were determined, respectively. To determine the edge energy, the fluorescence intensity was normalized by $dI_{\mathrm{Co}}/dE_{\mathrm{Ph}}$ and converted into an oxidation state change using the calibration obtained from reference XANES spectra of bulk powder of CoO and Co_3O_4 (Sigma-Aldrich) 5% diluted in cellulose pellets having the Co-oxidation states of 2 and 2.67, respectively.

Electrochemical Impedance Spectroscopy

Electrochemical impedance spectroscopy studies were carried out at the PETRA III beamline *P*23 during the *operando* SXRD measurements using the electrochemical cell described above. SXRD data were continuously acquired throughout the following electrochemical protocol: After an initial CV (0.97 to 1.77 V, 5 mV/s), impedance spectra were recorded at selected potentials. Here, the potential was ramped linearly to each measurement point and held for 10 s prior to acquiring an EIS spectrum. A subsequent CV was recorded after the measurement series to verify that no irreversible changes were induced during EIS. Impedance spectra were acquired with a Solartron ModuLab XM ECS potentiostat under potentiostatic bias in the frequency range of 1 MHz to 1 Hz using 20 points per decade and a sine wave amplitude of 5 mV. Before fitting, an Impedance Hilbert transform (Z-HIT) correction was applied to improve magnitude−phase consistency and mitigate the effect of artifacts arising from transient interfacial disturbances.[39] Impedance spectra were fitted in Python using the equivalent circuit shown in Figure 8c, employing the lmfit (https://lmfit.github.io/lmfit-py/fitting.html) library, considering the frequency range of 100 kHz to 1 Hz to exclude high-frequency artifacts. A least-squares algorithm with a non-negativity constraint and weighting (frequency$^{0.3}$) was employed. For the annealed films below 1.5 V, the inductive contribution was negligible and thus was constrained to 0 H to stabilize the fit. In this case, no additional frequency weighting was applied. The series resistance was fixed at 50 Ω for all data sets because the electrolyte conductivity was assumed to be constant, which was ensured by a continuous feed of fresh electrolyte.[40] Standard errors derived from the fit covariance matrix are shown as error bars in the respective figures. The robustness of subprocess deconvolution was evaluated via parameter−correlation analysis using the covariance matrix returned by *lmfit*.

RESULTS

Influence of Annealing on the Co Oxide Film Structure

We first describe the influence of thermal annealing on the structural properties of the electrochemically deposited Co$_3$O$_4$ film. According to initial studies, noticeable changes in the film morphology only occurred at temperatures ≥ 300 °C (see the Supporting Information, Figure S1). Therefore, annealing for 30 min at 400 °C in an Ar atmosphere was chosen as standard conditions, which is similar to the annealing steps used for PVD-prepared Co$_3$O$_4$ epitaxial films.[14−17] Annealing was performed both under Ar and synthetic air at atmospheric pressure, yielding identical results.

As described in our previous work,[10−13] the electrodeposition process results in epitaxial Co$_3$O$_4$(111) films with a defined in-plane orientation, in which the Co$_3$O$_4$[$\bar{2}\bar{2}4$] direction is aligned with the [$1\bar{1}0$] direction of the Au(111) substrate. The good alignment of the Au and Co$_3$O$_4$ lattice can be seen in the X-ray intensity distribution of Co$_3$O$_4$ peaks along the Au(01L) crystal truncation rod (Figure 1). The same lattice structure and orientation are found after annealing of the samples in air or in Ar, confirming that the material is stable under these conditions.

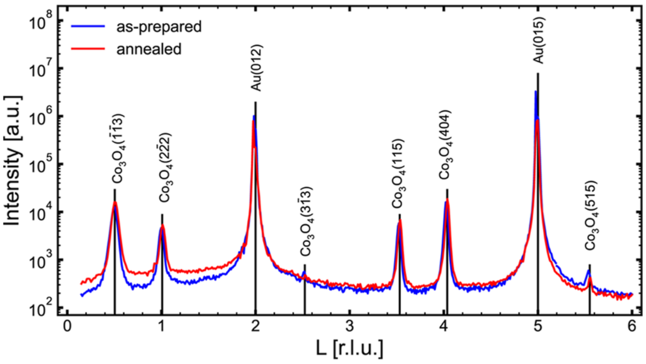

Figure 1. X-ray intensity distribution along the (0, 1, L) crystal truncation rod of the Au substrate, showing the Bragg peaks of Au and of the electrodeposited Co$_3$O$_4$ oxide film. The expected positions of (unstrained) Co$_3$O$_4$ Bragg peaks are indicated with solid lines and indexed according to the Co$_3$O$_4$ simple cubic unit cell. The Co$_3$O$_4$ film remains stable after annealing for 30 min at 400 °C in an Ar atmosphere.

In contrast, clear changes in the nanoscale morphology are observed upon annealing. Atomic-force microscopy (AFM) images of the as-prepared Co$_3$O$_4$ films, presented in Figure 2a,c, show the characteristic granular morphology found in our previous studies,[11−13] consisting of tightly packed triangular islands. The island edges are oriented at 60° with respect to each other, i.e., preferentially oriented along the main in-plane lattice directions. The lateral island size is ≤100 nm in these samples. The top of the islands is covered by small structures of ≤1 nm in height and several nanometers in width (Figure 2a,c, insets). After annealing, the islands have partially merged, although the average island size has not changed significantly. They exhibit a more rounded shape, and in some cases, even very well-developed hexagonal islands are observed (Figure 2d). Moreover, distinct grooves have opened up between the islands that can be up to 20 nm wide and up to 15 nm deep (measured depths, shown in the cross sections in Figure 2, are limited by the opening angle of the AFM tip and thus should be considered as a lower limit). The formation of these grooves may be due to the reorganization of the islands or to their volume contraction induced by the annealing, which will be discussed further below. Another striking difference is the top of the islands, which appear atomically smooth after annealing. Further support for such morphological changes comes from detailed *in situ* XRD studies during annealing (Supporting Information, Figure S2) that show that the average grain size along the surface normal direction first decreases with increasing annealing temperature and above 300 °C increases again. Despite these morphological changes, the roughness factors of the annealed films, obtained from the AFM images, are small and similar to those of the as-prepared samples (typically 1.01 to 1.10).

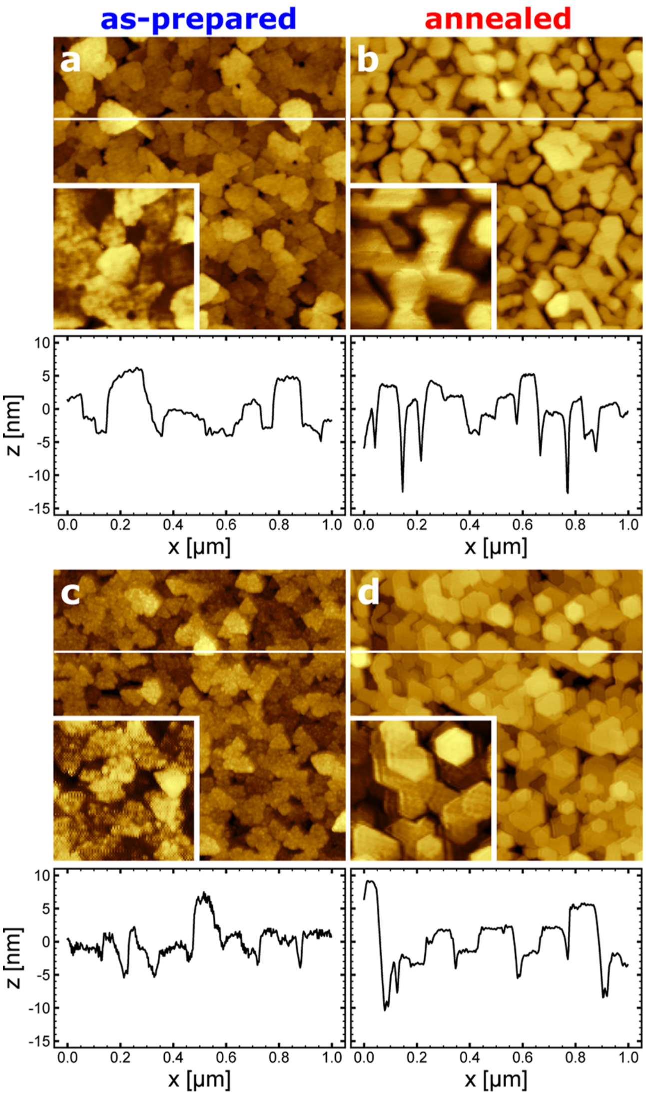

Figure 2. AFM images (1 μm × 1 μm) of two electrodeposited Co$_3$O$_4$ films on Au(111). (a,c) As-prepared samples and (b,d) after annealing of those samples for 30 min at 400 °C in (b) Ar and (d) synthetic air. Smoothening of the nanoscale roughness on top of the islands upon annealing can be seen in the insets (250 nm × 250 nm) and cross sections (taken at the positions of the white lines in the images); the latter also illustrate the formation of deep grooves.

In addition, we studied the effect of thermal annealing on the lattice structure and morphology of epitaxial CoOOH films electrodeposited on Au(111) (Figure S3). Here, annealing leads to a transformation of the epitaxial (0001)-oriented

CoOOH lattice of the as-prepared film into a $Co_3O_4(111)$ film with the same epitaxial relationship as that above. A similar phase transformation has been reported previously for micrometer-thick electrodeposits of $Co(OH)_2$ on Au(111), which transformed to epitaxial CoOOH(0001) and then to $Co_3O_4(111)$ films upon annealing in air at 95 and 300 °C, respectively.[41] Furthermore, this behavior is in agreement with thermochemical studies of Co oxides formed by precipitation from aqueous alkaline solutions, where a similar phase transition from CoOOH to Co_3O_4 and a concomitant release of H_2O and O_2 were observed at 300 °C.[42] The morphology of the $Co_3O_4(111)$ film formed by annealing of CoOOH differed noticeably from that formed by annealing of the Co_3O_4 electrodeposit. AFM images show islands with micrometer-sized lateral dimensions that exhibit a high density of nanoscale pores, often with triangular features (Figure S3b). The difference to annealed Co_3O_4 is not surprising, taking into account that also the as-deposited CoOOH and Co_3O_4 differ strongly in nano- to microscale morphology.[10,38] Furthermore, the 40% larger volume density of Co atoms in Co_3O_4 as compared to CoOOH (see discussion) can readily explain the observed porous structure.

Electrochemical Behavior

The electrochemical characterization of the Co oxide films was performed in the cell used for the *operando* SXRD studies as well as in a separate cell in which the samples were mounted on a rotating disk electrode (RDE). The RDE measurements allow us to overcome limitations of the previous studies of Co thin film electrodes by us[10−13] and others.[14−17] In particular, they enable the first measurements of these model catalysts under well-controlled mass transport conditions and at higher current densities.

As shown in Figure 3a, thermal annealing leads to pronounced changes in the electrochemical response in the potential regime negative of the onset of the OER, which is dominated by capacitive currents. The cyclic voltammogram (CV) of the as-prepared sample exhibits a large pseudocapacitive current over the entire studied range, with a transferred charge of approximately 5 mC/cm^2 between 0.9 and 1.6 V. After annealing, this current is reduced strongly, by up to one order of magnitude. Both the as-prepared and the annealed sample feature a redox peak at 1.54 V (in the following denoted as A2/C2 in accordance with the literature), which is well-known from previous work and most probably indicates formation of a surface oxyhydroxide species.[12,18] However, the charge transferred in this peak (determined from A2 after subtraction of the OER and the capacitive current) decreases from ~1.7 mC/cm^2 to ~230 μC/cm^2 upon annealing. The cathodic peak at 1.15 V may partly result from a second Co redox wave[7,43,44] but may in addition contain contributions from the reduction of Au oxide, which is formed during the positive sweep at exposed areas of the Au substrate within cracks of the Co_3O_4 film. On the basis of the charge of this peak, we estimate the exposed Au surface area of the Co_3O_4 film samples to be less than 10% (see Supporting Information, Section S2, Figure S4).

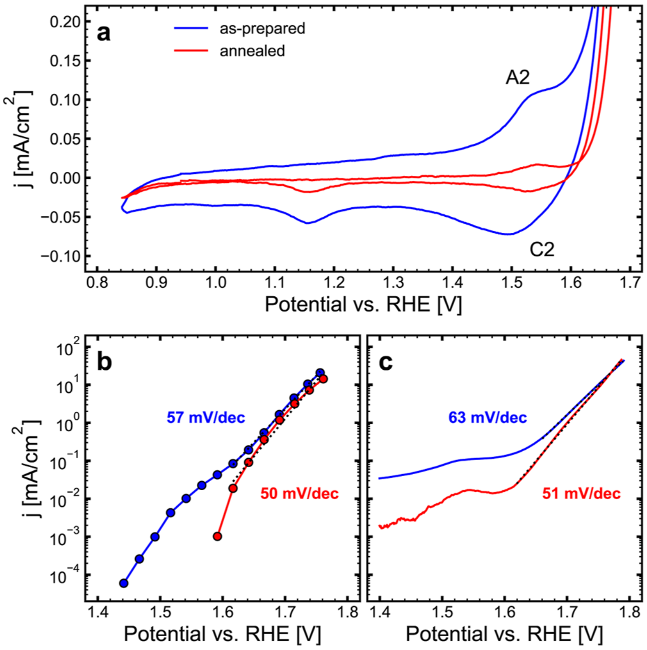

Figure 3. Electrochemical response of a $Co_3O_4(111)$ film in 0.1 M NaOH before and after annealing at 400 °C in Ar. The measurements were performed on an RDE at 3000 rpm. (a) Cyclic voltammogram measured at 5 mV/s, showing the capacitive potential range. (b,c) Tafel plots of the OER current density. The data correspond to (b) steady-state current density, obtained by stepwise increase of the potential every 4 min, and (c) current density during anodic potential sweeps at 5 mV/s.

Earlier studies of OER on Co thin film model catalysts were typically restricted to low current densities (in some cases even <1 mA/cm^2). The use of an RDE in this study allowed measurements over a large current density range, up to 20 mA/cm^2. Above 20 mA/cm^2, the currents became increasingly noisy due to bubble formation and detachment and were therefore not employed for the analysis. Figure 3b,c shows the OER current density obtained during anodic potential sweeps, as employed in earlier electrochemical studies of epitaxial Co_3O_4 films, as well as the true steady-state current density obtained by potential step experiments. Both are in good agreement for potentials positive of 1.65 V; at more negative potentials the anodic sweeps become dominated by the pseudocapacitive currents. Despite the large changes in the capacitive potential range, the OER activity of the as-prepared and annealed $Co_3O_4(111)$ films is similar. The Tafel slope of the as-prepared samples is typically close to 60 mV/dec, in agreement with our previous reports.[10,11] After annealing, a decrease in the Tafel slope by about 15% was consistently found. Simultaneously, the onset potential of the OER shifted slightly in the positive direction. As a result, annealing of the Co_3O_4 samples led to higher OER overpotentials at low current densities but equal or lower overpotentials in the range ≥10 mA/cm^2 used for technical applications. A decrease of the Tafel slope upon annealing was also found in potential-sweep measurements employing the cell used for the *operando* SXRD studies. However, the Tafel slopes in this case appeared slightly larger due to mass transport limitations.

The electrochemical measurements indicate that annealing results in a significant change of the Co_3O_4 samples' state. To determine the long-term stability of the as-prepared and the annealed sample state under OER conditions, we studied the electrochemical response for both types of samples over time periods of up to 80 h. These experiments were performed at 5 mA/cm^2 in the SXRD cell under continuous exchange of the electrolyte solution to ensure that the electrolyte composition remained constant and to remove O_2 bubbles. Interestingly, both types of samples are quite stable over the course of these experiments. As can be seen in Figure 4, the current in the capacitive potential range between 0.9 and 1.4 V remains rather constant in both cases (see also CVs in the Supporting Information, Figure S5). Specifically, the large pseudocapacitive current density, which is characteristic of the as-prepared state, and the much lower current density of the annealed sample are both maintained. Furthermore, also the characteristic morphology of the as-prepared and the annealed samples is maintained (Figure S6). This indicates that both of these states are stable over these time scales even under an OER operation at rather high rates. It is noted that for the as-prepared sample, the redox peak A2/C2 initially increases, which is in accordance with an increasing amount of surface restructuring found in the SXRD studies (see below). Furthermore, the onset of the OER appears to shift to more negative values for both as-prepared and annealed samples, suggesting additional activation of the catalyst. In view of the limited long-term stability of the Ag/AgCl reference electrode in these preliminary long-term experiments, we refrain from a quantitative interpretation of these shifts. Further, more detailed studies are required for investigating the evolution of the OER behavior of these model catalysts.

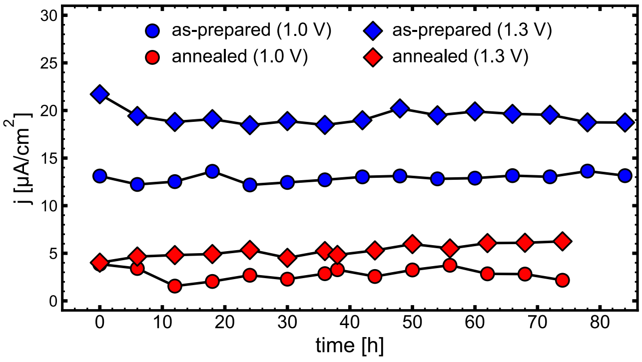

Figure 4. Electrochemical long-term studies of as-prepared and annealed $Co_3O_4(111)$ films in 0.1 M NaOH. The figure shows the capacitive current density at 1.0 V (circles) and 1.3 V (diamonds), obtained from CVs at 5 mV/s, as an indicator for the sample state (see Supporting Information, Section S2 for details). In between the CVs, the sample was kept in the OER range at a constant current density of 5 mA/cm^2. The time axis indicates the duration for which the sample was exposed to the chronopotentiometric conditions. Both the as-prepared and the annealed sample maintain a constant high and low capacitive current density, respectively, indicating that both states are stable over these time scales.

Electrochemical studies of CoOOH films show a very similar behavior of the samples before and after annealing (Supporting Information, Figure S7a). As found in previous studies,[10,12] CVs of the as-prepared samples feature a low, rather uniform current density over the entire capacitive potential range without any distinct redox peaks. The pseudocapacitive current at 1.0 V is ∼5 μA/cm^2 (at 5 mV/s), i.e., almost identical to that found on annealed $Co_3O_4(111)$ films (see Figure 4). The CV of the annealed CoOOH film is similar to that of the as-prepared sample but exhibits a slightly higher current density in the capacitive range, which is probably caused by the larger electrochemical surface area resulting from the formation of pores (see Figure S3b). However, the CV now exhibits a redox peak at 1.54 V, albeit much weaker than that on the annealed $Co_3O_4(111)$ film. Taking into account that both the crystal structure and the morphology of the film are completely changed, the minor effect of annealing on the capacitive electrochemical response in the pre-OER regime is surprising. Furthermore, annealed $Co_3O_4(111)$ films have, apart from the small A2/C2 peak, a capacitive response very similar to that of the as-prepared CoOOH(001) films, which will be addressed further in the discussion section.

Operando SXRD Studies

Operando studies by surface X-ray diffraction reveal an extremely strong effect of annealing on the lability of $Co_3O_4(111)$ with respect to structural surface transformations. This effect is illustrated exemplarily in Figure 5 where the changes in Co_3O_4 lattice strain within ($\varepsilon_\parallel$) and normal to ($\varepsilon_\perp$) the surface plane, and the in-plane ($d_\parallel$) and out-of-plane ($d_\perp$) grain sizes are shown together with the simultaneously measured electrochemical current and optical reflectivity. The as-prepared $Co_3O_4(111)$ film exhibits the pronounced potential-dependent changes reported in our previous studies.[10−13] In particular, the grain size decreases due to the

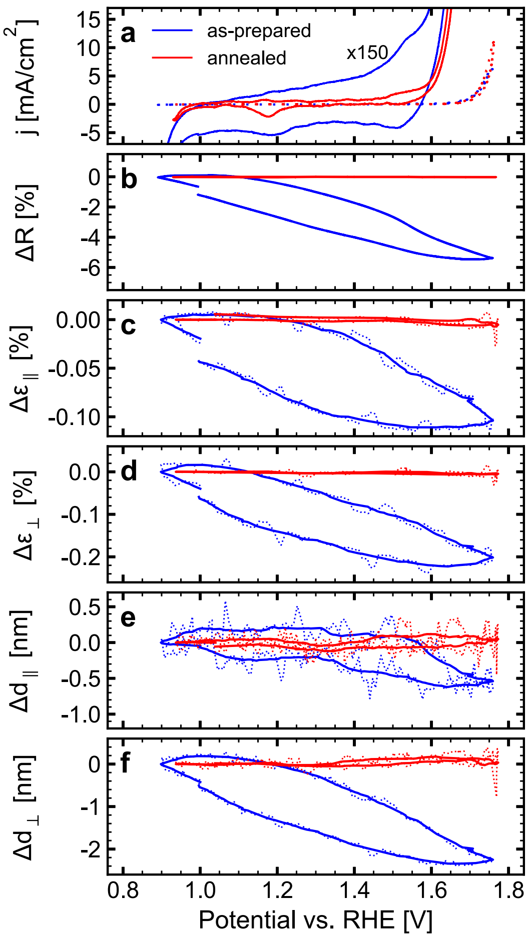

Figure 5. (a) CV, (b) optical reflectivity, and (c−f) *operando* SXRD data for an as-prepared $Co_3O_4(111)$ film of 60 nm thickness (blue) and for the same film after annealing at 400 °C in Ar (red), recorded simultaneously in 0.1 M NaOH during potential cycles at 5 mV/s. Shown are (from top to bottom) the electrochemical current density j, the change in optical reflectivity ΔR, the changes in in-plane and out-of-plane lattice strain $\Delta\varepsilon_\parallel$ and $\Delta\varepsilon_\perp$, and the changes in average in-plane and out-of-plane grain size $\Delta d_\parallel$ and $\Delta d_\perp$ of the Co_3O_4 film (given with respect to the values at 0.9 V). In (c−f), the dotted lines correspond to the raw data and the solid lines to data smoothened by a Savitzky−Golay filter with a width of ∼150 mV.

transformation of the Co_3O_4 near-surface region into the skin layer phase. In parallel, the formation of the skin layer induces a contraction of the underlying Co_3O_4 lattice.[11] For the employed films, which consist of planar $Co_3O_4(111)$ islands with in-plane sizes of ∼100 nm, the strain and grain size changes in the surface-normal direction are significantly larger than the in-plane changes. This effect was already described in ref 13 and can be explained by a scenario where the skin layer is formed on the top surface and the outer island walls, but not at in-plane grain boundaries within the islands.

The skin layer formation commences at about 1.15 V, where in particular, $d_\perp$ and $\varepsilon_\perp$ start to change noticeably. In the potential region above 1.5 V, i.e., near the distinct redox peak A2/C2, the slope of these changes increases, and also $d_\parallel$ starts to decrease, together with an increased change in $\varepsilon_\parallel$. This two-stage growth behavior of the skin layer was already found in previous studies of this system.[13] Apart from some hysteresis, these structural changes are highly reversible. Combined XRD/XAS studies have shown that all Co^{2+} species in the skin layer are converted to Co^{3+}.[12] The pseudocapacitive current can be attributed to the charge transfer associated with this oxidation state change. Furthermore, the optical reflectivity (R) has been shown to mirror the pseudocapacitive charge transfer in these films.[10] Close inspection of j and ΔR in Figure 5 indicates significant changes in the positive sweep only above 1.15 V, whereas in the negative direction the changes are found down to 0.9 V. This behavior is in excellent agreement with the hysteresis in the formation of the skin layer and its subsequent reduction back to Co_3O_4 observed in the simultaneously obtained structural data under these potentiodynamic conditions. Depending on the preparation, the changes in $d_{\perp,\parallel}$ and $\varepsilon_{\perp,\parallel}$ remain similar or increase in successive potential cycles. In the latter case, the increase occurs primarily in the region of redox peak A2/C2 and is accompanied by an increase in the intensity of this peak, indicating an increasing average thickness $\langle d_{skin} \rangle$ of the skin layer (see Supporting Information for the definition of $\langle d_{skin} \rangle$, Section S4).

After annealing of the sample, no potential dependent changes in the grain size and strain are observable within the experimental accuracy of the measurements. In particular, the vertical Co_3O_4 grain size $d_\perp$ remains constant within ±0.1 nm. The latter observation suggests that at the (111)-oriented surface on top of the annealed Co_3O_4 grains, no restructuring of the spinel lattice occurs, with the possible exception of minor relaxation of the positions of the surface atoms. According to these data, the thermal treatment effectively suppresses the formation of the skin layer, i.e., leads to a significant stabilization of the Co_3O_4 surface structure against surface transformation. In some SXRD experiments, some minor changes of the strain, in particular $\varepsilon_\parallel$, and the optical reflectivity (R) were observed, suggesting that minor skin layer formation may still occur (Supporting Information, Figure S8), but the grain sizes remained constant within the experimental accuracy of ±0.1 nm. These residual changes may be caused by insufficient annealing.

The suppression of Co_3O_4 skin layer formation by annealing is in good agreement with the strong decrease in the pseudocapacitive current in the capacitive potential range and the suppression of potential-dependent changes in the optical reflectivity. The absence of substantial changes in R for the annealed films therefore suggests that, similar to CoOOH(0001),[12] the transferred pseudocapacitive charge is small and has to be restricted to oxidation state changes at the oxide surface. Support for the latter comes from combined *in situ* SXRD and X-ray absorption spectroscopy measurements on a Co_3O_4 film before and after annealing (Figure 6). The increase in the oxidation state of the as-prepared film between 1.0 and 1.6 V is in good accordance with a change of Co^{2+} cations in the 1 nm thick skin layer region to Co^{3+}, as already found in ref 12. In addition, the most pronounced changes in oxidation state are present in the potential region of the A2/C2 redox peak, in agreement with the more pronounced skin layer growth in this region. In contrast, the oxidation state changes after annealing of the film are a factor of 3 lower. Considering that 1 nm of Co_3O_4 corresponds to approximately 3 layers of Co cations, this result indicates that in annealed Co_3O_4 the change in oxidation state is largely limited to the outermost surface layer of the film.

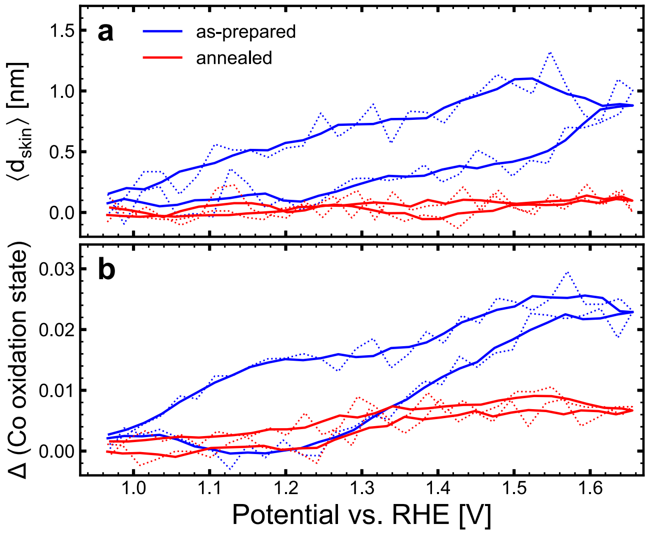

Figure 6. Potential-dependent changes of the average skin layer thickness (a) and of the average Co oxidation state (b) of a $Co_3O_4(111)$ film in its as-prepared state (blue) and after annealing (red), obtained by combined *in situ* SXRD and X-ray absorption spectroscopy measurements (dotted and solid lines correspond to raw and smoothened data, respectively). The factor of three lower change in oxidation state of the annealed film is in accordance with the negligible skin layer formation and indicates that only Co atoms at the oxide surface are oxidized. As a reference point, the data at 1.0 V are used, where the total Co_3O_4 film thickness was 29 nm.

In our previous study,[11] we found that the OER activity at low overpotentials increases with the average thickness $\langle d_{skin} \rangle$ of the skin layer. We confirmed this result by *operando* SXRD studies of as-prepared $Co_3O_4(111)$ films with different $\langle d_{skin} \rangle$ values as well as the corresponding annealed films. This is illustrated in Figure 7 where we show as a function of $\langle d_{skin} \rangle$ the overpotential at an OER current density of 1 mA/cm^2, i.e., as in ref 11, as well as at 0.2 mA/cm^2 and 5 mA/cm^2. In some experiments, where the thickness of the skin layer increases over time (blue circles and squares), the decrease in overpotential with increasing $\langle d_{skin} \rangle$ can be followed directly on the same sample. On the annealed films, $\langle d_{skin} \rangle$ is close to zero for all samples, independent of the skin layer thickness observed prior to annealing. The OER overpotentials of the annealed samples are identical within ±10 mV, which is the accuracy of the potential measurements in the *operando* SXRD cell (see Supporting Information, Section S2). At low OER current density, annealing increases the OER overpotential (up

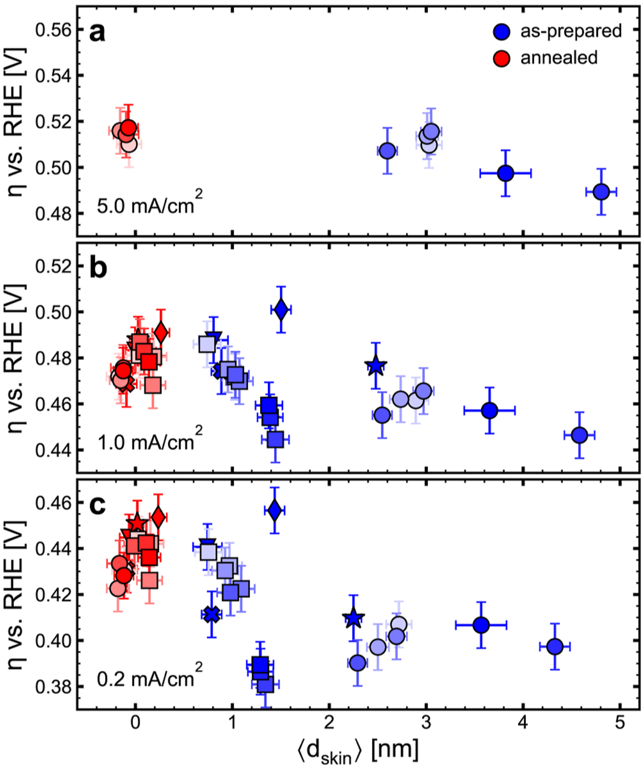

Figure 7. Correlation of the skin layer thickness with the OER activity of different $Co_3O_4(111)$ films. The average thickness $\langle d_{skin} \rangle$ was obtained from the *operando* SXRD data and the OER overpotentials at (a) 5 mA/cm^2, (b) 1 mA/cm^2, and (c) 0.2 mA/cm^2 from the anodic sweeps of the simultaneously recorded CVs. The data originate from experiments on a number of different thin film samples (indicated by different symbol shapes), each measured multiple times during the SXRD experiment (order of measurements indicated by color, with darker colors corresponding to later times in the experiment).

to 60 mV at 0.2 mA/cm^2). However, at 5 mA/cm^2, as-prepared and annealed samples have similar OER activity. Only for samples with very large $\langle d_{skin} \rangle$ values are noticeable lower overpotentials found. These observations are in full agreement with the results of the RDE studies, which indicate an intersection of the OER currents of as-prepared and annealed samples at large current densities. They demonstrate that the beneficial effect of the surface structural transformation is limited to low overpotentials.

Similar *operando* studies were also performed for CoOOH(0001) films (Supporting Information, Figure S7), which are already perfectly stable in the as-prepared state.[10] Unsurprisingly, the $Co_3O_4(111)$ films formed by the annealing of those samples also do not exhibit changes in strain, grain size, and optical reflectivity. This is in agreement with the very similar electrochemical response recorded before and after annealing.

Correlative EIS Studies

The *operando* SXRD studies described above were augmented by detailed EIS characterization over a wide potential range. The combination of these techniques enables an unambiguous correlation between structural evolution and electrochemical behavior, providing mechanistic insights into how surface transformations affect the OER activity. To verify the validity of these EIS data, obtained at the synchrotron in the *operando* SXRD cell, we additionally performed similar studies in the RDE cell (see Supporting Information, Figures S11 and S17 for results obtained on the sample studied in Figure 3).

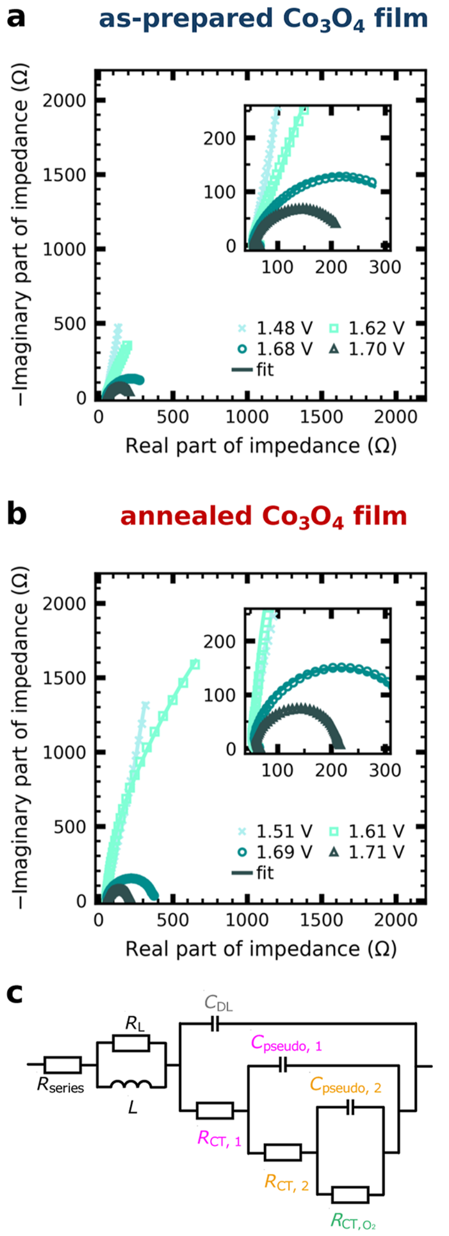

Figure 8. Electrochemical impedance spectra of (a) as-prepared $Co_3O_4(111)$ film shown in Figure 5 and (b) same film after thermal annealing, measured at selected DC operating potentials. The Nyquist plots are shown together with equivalent circuit fits (solid lines) based on a previously established model for normal spinels in alkaline electrolyte, illustrated in (c). The three-ladder circuit enables deconvolution of the charge transfer resistances ($R_{CT,1}$, $R_{CT,2}$, and R_{CT,O_2}) and (pseudo)capacitances (C_{DL}, $C_{Pseudo,1}$, and $C_{Pseudo,2}$). Additional circuit elements (resistances R_{series} and R_L, as well as inductance L) are included to account for contributions arising from the cell setup rather than interfacial electrochemical processes.

Figure 8a,b shows impedance spectra recorded at different potentials for a $Co_3O_4(111)$ film before (a) and after (b) thermal annealing. In both cases, the spectra exhibit a slightly tilted line nearly parallel to the negative imaginary axis in the capacitive region. At more anodic potentials, where the OER

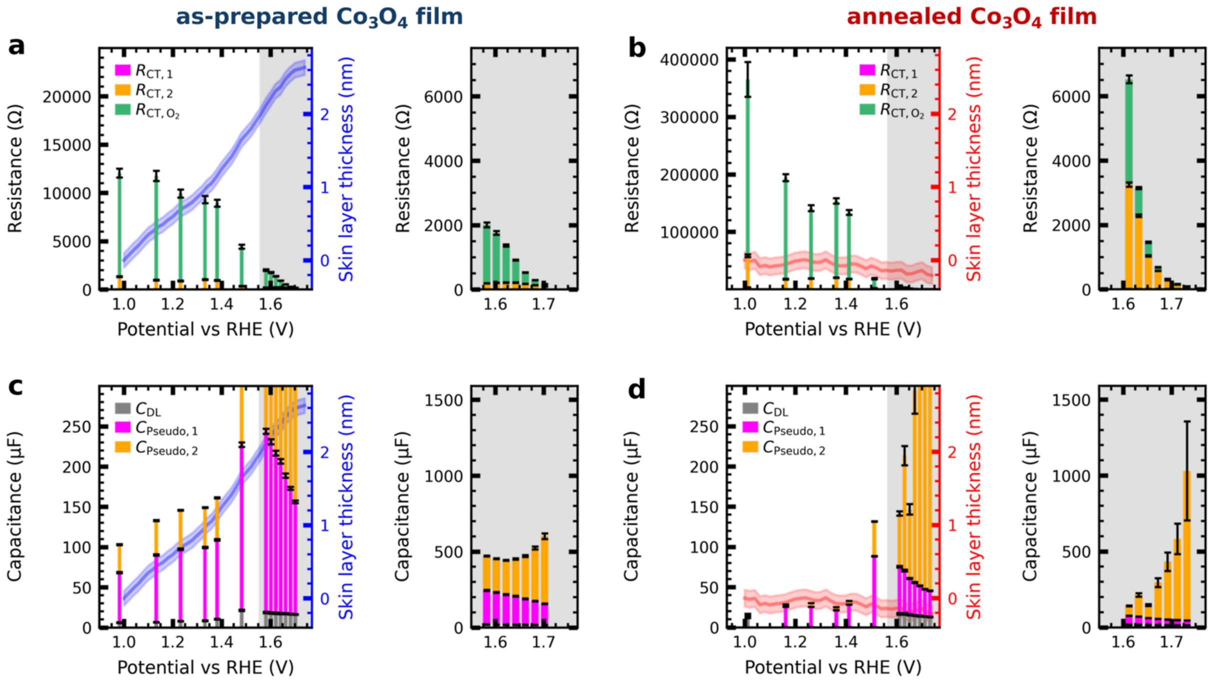

Figure 9. Potential-dependent (a,b) charge-transfer resistances and (c,d) (pseudo)capacitances of the $Co_3O_4(111)$ film studied by the *operando* SXRD measurements shown in Figure 5. The data are obtained (a,c) before and (b,d) after thermal annealing. The secondary axes of the full-range plots indicate the average skin layer thicknesses, which are included in the plots as blue and red lines, respectively.

current increases, this feature evolves into a semielliptical shape composed of overlapping semicircles (see Figure S9 for the complete set of impedance spectra). The zoomed-in insets further reveal an inductive loop in the high-frequency region (detailed in Figure S10), which likely originates from the *operando* cell setup, as its shape varied under different measurement conditions and was not observed in the RDE cell (Figure S11). Notably, the inductive contribution diminished after thermal annealing of the Co_3O_4 film, suggesting that a relation to the interfacial properties of the film cannot be ruled out.

For quantitative analysis of the EIS data, equivalent circuit fitting was performed using a previously developed model for normal spinel catalysts in alkaline electrolyte (Figures 8c and in S12 in comparison to alternative models),[45−47] supplemented by a parallel RL element to account for the high-frequency inductive loop. The interfacial subprocesses are represented by a nested three-ladder circuit comprising the double-layer capacitance C_{DL} and two pseudocapacitive elements $C_{Pseudo,1}$ and $C_{Pseudo,2}$, which are charged through the charge transfer resistors $R_{CT,1}$ and $R_{CT,2}$, respectively. We relate the pseudocapacitive subprocesses to the formation of intermediate states,[48] which refers to coupled oxidation of cobalt sites and the adsorption of oxygen-containing species or their further reaction once adsorbed. Specifically, $R_{CT,1}$ and $C_{Pseudo,1}$ are assigned to the Co^{2+}/Co^{3+} transition, while $R_{CT,2}$ and $C_{Pseudo,2}$ correspond to the Co^{3+}/Co^{4+} transition. The charge transfer resistance $R_{CT,\,O_2}$ is attributed to the subsequent formation and desorption of molecular oxygen. The corresponding circuit element can thus be interpreted as the leakage resistor of the second pseudocapacitor. Further details on the rationale for the circuit model selection are provided in the Supporting Information (Section S6).

Figure 9 summarizes the deconvoluted resistive and capacitive contributions for the Co_3O_4 film before and after annealing along with the progression of the average skin layer thickness. At each operating potential, the partial resistances and capacitances are shown as stacked bars, allowing the total value to be readily assessed alongside the individual contributions. The complete set of results is provided in Figure S17, which includes plots for the individual circuit elements, a measurement series on a second film that exhibited less pronounced skin layer formation, and a film characterized in the RDE setup. Both the total capacitances and resistances in Figure 9 exhibit the potential-dependent trends anticipated from the cyclic voltammograms (Figure 5a), while the correlation matrices of the deconvoluted parameters reveal no systematic or dominant interdependencies.

The double-layer capacitance is considerably smaller than the pseudocapacitive contributions. Among these, $C_{Pseudo,1}$ dominates in the capacitive potential range, where it peaks in a similar region as the pseudocapacitive current observed in the voltammogram (Figure 5a). At more anodic potentials, it then decreases. In contrast, $C_{Pseudo,2}$ increases in the OER potential range and eventually surpasses $C_{Pseudo,1}$, consistent with the behavior described for several hydrous transition metal oxides.[49] The potential ranges of the capacitance profiles for both pseudocapacitive elements remain essentially unchanged before and after thermal annealing, but their magnitudes are strongly affected. After annealing, $C_{Pseudo,1}$ is smaller by a factor of 3 and $C_{Pseudo,2}$ decreases even more prior to the OER range. Although the roughness of the Co_3O_4 crystallites decreases as a result of thermal treatment, the associated change in surface area cannot explain alone the large decrease in the pseudocapacitance values. For the as-prepared film, the cumulative sum of $C_{Pseudo,1}$ roughly follows the skin layer thickness. After annealing, $C_{Pseudo,1}$ is significantly reduced across the entire investigated potential window, reflecting suppression of the skin layer formation. $C_{Pseudo,2}$ is likewise suppressed in the capacitive region but recovers to values comparable to the as-prepared sample at OER potentials, suggesting that it is only indirectly related to skin layer formation. A second Co_3O_4 film, which exhibited a lower extent of skin layer formation (Figure S8), also showed a lower total capacitance in the capacitive potential range. In this range, $C_{\mathrm{Pseudo},1}$ was again the dominant contribution and decreased markedly upon thermal annealing (Figure S17, sample 2).

Before and after annealing (Figure 9a,b), the total interfacial resistance is very high in the capacitive region and decreases exponentially at more anodic potentials associated with oxygen evolution. Among the individual contributions, $R_{\mathrm{CT},1}$, related to mutual OH^- adsorption and Co^{2+} oxidation, is at least one order of magnitude smaller than the others. By contrast, R_{CT,O_2}, assigned to oxygen release, dominates across most of the investigated potential range, and for the as-prepared film, even at all measured OER potentials. The resistance $R_{\mathrm{CT},2}$ characterizes the kinetic hindrance of the second pseudocapacitive charging process, in which Co^{3+} sites are oxidized alongside an OER reaction step. Within the examined OER potential window, $R_{\mathrm{CT},2}$ is smaller for the as-prepared film and becomes similar to R_{CT,O_2} at the most positive potentials. However, after thermal annealing, $R_{\mathrm{CT},2}$ accounts for the largest portion of the interfacial resistance. As shown in Figure S17b, within the capacitive potential range, $R_{\mathrm{CT},2}$ has a dip, where the A2 peak is observed in the CV and then decreases exponentially at higher overpotentials. While initially lower for the as-prepared film, $R_{\mathrm{CT},2}$ for as-prepared and annealed samples overlaps at elevated overpotentials. R_{CT,O_2} is likewise smaller for the as-prepared sample at low overpotentials but decreases more rapidly after thermal annealing at large overpotentials, consistent with the higher catalytic current observed in this potential range for annealed samples. For both preparation conditions, R_{CT,O_2} decreases more steeply with potential than for $R_{\mathrm{CT},2}$, implying that the relative contribution of $R_{\mathrm{CT},2}$ may further increase at even higher potentials.

DISCUSSION

Annealing-Induced Changes in Catalyst Structure and Reactivity

The as-prepared $Co_3O_4(111)$ films undergo substantial structural changes upon annealing. First, the islands change from a more triangular shape to a rounded shape. The electrodeposition process results in (depending on the deposition conditions) more or less well-developed triangular islands with two twin-related lattice orientations that are parallel or antiparallel with respect to the Au(111) substrate.[38] The edges of these triangular islands may be either (111) or (100) facets. The observation that the Co_3O_4 film is electrodeposited on all surfaces, including Au(100) substrates,[11] as a (111)-oriented film, indicates that $Co_3O_4(111)$ is the surface with the slowest growth rate and defines the growth front. Consequently, it seems likely that the island edges correspond to the (111) facets. Annealing should result in a structure that is closer to the Co_3O_4 equilibrium shape, in which, under oxidizing conditions, oxygen-terminated (111) and (100) facets coexist according to DFT calculations.[50] This is in full agreement with the observed hexagonal island shape.

The AFM images indicate that the top of the electrodeposited Co_3O_4 islands is highly defective and exhibits a roughness in the range of 1 nm. This roughness may be related to the low temperature as compared to UHV-prepared films. It is therefore likely that also the (111)-oriented island edges exhibit a comparable roughness. Thermal annealing increases the surface mobility and allows healing of these defects as observed in the AFM images. As comparable annealing is also used as the last step in the preparation of $Co_3O_4(111)$ films by PVD, we expect to obtain a similar, atomically smooth structure as found under UHV conditions.[14−17]

While the effects described above can account for the changes in the Co_3O_4 island morphology, they cannot explain the formation of deep grooves between the islands after thermal annealing. The latter may be due to changes in the island volume, which we assign to chemical transformations. Specifically, we assume that the Co_3O_4 film in the as-prepared state contains a fraction of hydroxide species. This is supported by detailed XAS studies, which show that as-prepared $Co_3O_4(111)$ films have an oxidation state 3% lower in air than once in contact with electrolyte.[12] This suggests that around 10% of Co atoms in the film have an oxidation state +2. This can be due to the presence of O vacancies or a layer of $Co(OH)_2$. In the case of a hydroxide layer, conversion to Co_3O_4 upon annealing will result in a 46% reduction in volume, which could account for the decrease in the volume of the three-dimensional islands. At the temperature of 300 °C, we indeed observe a vertical compression of the grains and major changes in the island morphology (Figures S1 and S2). This suggests that the hydroxide layer hypothesis is more likely. The hydroxide layer is also modified under electrochemical conditions and becomes more Co_3O_4-like.[12] This transformation probably contributes to an increased defect density on the surface.

The surface structure differences between the as-prepared electrodeposited and the annealed Co_3O_4 film can explain the very different lability toward skin layer formation. According to our SXRD studies, annealed $Co_3O_4(111)$ is stable against this surface structural transformation. Consequently, water and OH^- ions only adsorb on this surface but do not initiate the skin layer formation. Previous UHV spectroscopic studies[17,51] and *ab initio* theory[29,30] provided strong evidence for the hydroxylation of $Co_3O_4(111)$, even at very low water vapor pressure. According to the DFT study by Yan and Sautet,[29] this surface is over a wide range of H_2O and O_2 partial pressures of 1 to 10^{-6} bar in a state where a significant fraction of the surface oxygen is hydroxylated and surface Co in tetrahedral sites becomes octahedrally coordinated by chemisorbed water. A similar behavior was found in molecular dynamics studies of $Co_3O_4(100)$ surfaces, specifically a strong hydroxylation of surface oxygen groups and a higher local OH coverage around the tretrahedral Co^{2+}.[30] These results are consistent with a recent *in situ* X-ray photoelectron spectroscopy study of epitaxial $Co_3O_4(111)$ films in 0.5 mbar H_2O vapor.[52] Following the results of ref 29, a well-ordered hydroxylated $Co_3O_4(111)$ surface will expose only octahedrally coordinated Co to the electrolyte and is in this respect similar to the CoOOH(0001) surface, albeit the exact structural arrangements of the Co atoms at these two surfaces differ. In an electrochemical environment, the degree of hydroxylation will depend on the potential. With increasing potential the surface termination will gradually shift from an OH to an O-terminated surface, as has been shown by DFT[25] and *in situ* XAS studies of CoOOH(0001) films.[12] This potential-dependent deprotonation of surface hydroxyl groups via coupled proton−electron transfer accounts for the residual low capacitive current. Considering the similar surface density of oxygen groups on the (defect-free) CoOOH(0001) (1.42×10^{15} cm^{-2}[10]) and the hydroxylated Co_3O_4(111) surface (1.68×10^{15} cm^{-2} for the hydroxylated surface structure proposed in ref 29, assuming that no charge transfer to the chemisorbed water occurs), it is not surprising that both exhibit comparable current densities in the capacitive potential range, which are both much lower than those on the skin layer covered surface.

As the ideally terminated Co_3O_4(111) surface is structurally stable in the pre-OER and OER potential range, the observed skin layer formation on the as-prepared Co_3O_4 film has to be assigned to a phase transformation which starts at defects and proceeds over distances of a few nanometers into the lattice. In particular, we believe this process to occur at step edges, based on our previous studies that reveal a larger average skin layer thickness for films consisting of small three-dimensional islands than for films with larger flat-top islands.[11] The proposed process should result in a Co_3O_4(111) surface that is partially covered by the disordered oxyhydroxide phase. Subsequent decrease of the potential will revert this process, resulting in local recrystallization of the oxyhydroxide to Co_3O_4. Since the temperature is even lower than during the actual electrodeposition process, a similar rough surface morphology will result. This explains why the skin layer formation is highly reversible in successive potential cycles. In the potential region of the redox peak A2/C2, enhanced skin layer formation is observed in the *operando* SXRD data (Figures 5 and S8), especially in the lateral direction. The latter suggests that in particular, skin layer growth at the edges of the Co_3O_4 islands occurs in this region. For the case of the annealed Co_3O_4(111) film, where no skin layer is formed, the experimentally measured charge transfer of 230 μC/cm^2 in A2/C2 has to be attributed to changes in the oxidation state of surface species, such as oxidation of Co^{2+} to Co^{3+} and deprotonation of surface oxygen atoms. Alternatively, this peak may also be caused by a Co^{3+}/Co^{4+} redox reaction of the surface atoms, as proposed in earlier studies.[7,8,43,44] However, our *in situ* XANES measurements provide no evidence for (stationary) Co-oxidation states higher than Co^{3+} in this range.

The observed long-term stability of the voltammogram of the annealed Co_3O_4(111) film indicates that exposure to the electrochemical environment does not lead to significant formation of surface defects, even at potentials deep in the OER range (see Figure S5). *Vice versa*, the defective as-prepared Co_3O_4 films remain defective, i.e., no healing of surface defects occurs. Instead, potential cycling into the OER region may lead to a more defective surface, as suggested by the observed increase in $\langle d_{\mathrm{skin}} \rangle$ (see Figure 7) and the redox peak charge (see Supporting Information, Figure S5). Consequently, both types of surfaces correspond to qualitatively different states of the catalyst that are maintained under the operating conditions.

Finally, we note that calcination by thermal treatment is a standard process in the preparation of many (electro)catalysts, typically employed for the conversion of bulk structural phases and the decomposition or removal of reactants. According to our study, this process can also help to remove surface defects and to stabilize specific facets. Although this is not unexpected, a detailed understanding of these different roles of catalyst treatment is largely missing. *Operando* model catalyst studies as performed here may allow clear-cut studies on the influence of surface treatment methods and parameters on the surface defect structure. In addition to pure thermal annealing, which stabilizes well-ordered crystalline facets, other surface preparation methods, such as electron or ion irradiation or plasma treatments, may create defects that would allow skin layer formation. Systematic studies using thin-film model catalysts may allow evaluation of such surface engineering methods.

Oxygen Evolution Reaction

Our electrochemical studies indicate clear differences between the as-prepared and annealed Co_3O_4(111) film, which can be linked to the structural differences discussed in the previous section. The annealed samples, which are smooth and structurally stable, exhibit very well-defined uniform Tafel behavior that represents the activity of an ideal Co_3O_4(111) surface. In contrast, the OER activity of the as-prepared films increases with average thickness of the formed skin layer, which is in accordance with our previous work.[11] Based on this correlation, it was suggested that the entire skin layer is an OER-active reaction zone. Our new results indicate that this beneficial role of the skin layer is limited to low overpotentials. At higher overpotentials, the lower Tafel slope of the annealed Co_3O_4 samples leads to a crossover into a regime where the defect-free Co_3O_4(111) surface becomes more active than the skin layer phase.

Insight into the origin of the different catalytic activity at low and high overpotentials is provided by correlative EIS measurements determining contributions of interfacial subprocesses. The pseudocapacitive properties of normal cobalt spinel catalysts in alkaline solution typically give rise to distinguishable time constants, enabling the analysis of charge transfer resistances related to (1) simultaneous association of oxygen-containing electrolyte species and oxidation of Co^{2+} sites ($R_{\mathrm{CT},1}$), (2) further oxidation of the formed intermediate states consisting of cobalt sites and adsorbed O-intermediates ($R_{\mathrm{CT},2}$), and (3) the oxidative formation of oxygen and its release ($R_{\mathrm{CT},\,O_2}$). It should be noted that we do not attempt to distinguish between the many specific OER pathways[32] but rather provide information on how general stages of the OER are coupled to cobalt site oxidation and contribute to the overall rate limitation. According to our studies, $R_{\mathrm{CT},2}$ and $R_{\mathrm{CT},\,O_2}$ are the main contributions to the kinetic hindrance of the OER on Co_3O_4(111) films. Within the investigated OER potential range, the interfacial resistance is dominated by $R_{\mathrm{CT},\,O_2}$ for as-prepared films, whereas for thermally annealed films, it is governed by $R_{\mathrm{CT},2}$, with $R_{\mathrm{CT},\,O_2}$ decreasing more rapidly with increasing potential. Consequently, the reduced catalytic activity of the annealed film at low overpotentials can be attributed to the sluggish oxidation of the intermediate state comprising Co^{3+} sites. On the defect-free surface, the Co^{3+}/Co^{4+} transition is likely inhibited due to the lower number of electrochemically active sites and the lack of structural lability required to promote redox transformations. Nevertheless, in the logarithmic representation, the negative slope of $R_{\mathrm{CT},\,O_2}$ with increasing potential is steeper for the annealed film than for the as-prepared state, while $R_{\mathrm{CT},2}$ becomes comparable at higher overpotentials. As a result, the annealed film exhibits a higher OER activity in this regime. This may indicate a different mechanism or a different balance of competing pathways for the final steps of the OER on annealed films, consistent with the lower Tafel slope observed in Figure 3b,c. The inhibition of further oxide transformations may favor further reaction and desorption of oxygen-containing intermediates adsorbed only on outer surface cobalt sites since their incorporation into or stabilization within, e.g., highly hydroxylated phases, is suppressed. For the as-prepared $Co_3O_4(111)$ film, the higher OER activity at low overpotentials compared to the annealed state is linked to the more facile oxidation of Co^{3+} sites on the disordered, defective skin layer, reflected by the small contribution of $R_{CT,2}$. This facilitated Co^{3+} oxidation may appear connected to the extent of skin layer formation and, thus, to the pseudocapacitance $C_{Pseudo,1}$, for two reasons. First, a higher number of electrochemically active cobalt sites in a three-dimensional interfacial reaction zone may undergo the additional pseudocapacitive charging process. Second, structural disorder and defects may promote the formation of intermediate states involving Co^{4+}. However, if Co^{4+} and Co^{3+} sites are stabilized too strongly at more anodic potentials, this could hinder the final steps of the OER, which we assume are coupled to the self-discharge of active cobalt sites. This may also explain the less pronounced decrease of $R_{CT,\,O_2}$ with potential for the as-prepared film. In the framework of transformation lability,[35] these findings highlight the importance not only of facilitating the formation of oxidized active sites but also of enabling their internal reduction, thereby regenerating the initial active centers to sustain the catalytic cycle.

The possibility of preparing defect-free $Co_3O_4(111)$ electrodes that remain structurally stable for a long time and over a wide potential range is also of relevance for obtaining a fundamental understanding of the OER reaction on oxide catalysts. In particular, it enables a direct comparison of experiments on structurally well-defined model catalysts with results from *ab initio* modeling. As the latter typically requires in-plane order, the availability of ordered, crystalline oxide surfaces that are active and do not restructure is an important prerequisite for testing predictions of the OER mechanisms by *ab initio* theory.

CONCLUSION

The detailed correlative structural and electrochemical results obtained in our study provide important insights into the origin of the potential-induced surface restructuring of Co oxide electrocatalysts and the influence of this restructuring on the electrochemical response and the OER activity. We have shown that, first, not all Co_3O_4 electrodes are prone to surface restructuring and, second, that a lability toward structural transformation is not necessarily a prerequisite for high activity of the electrocatalyst. Instead, a more differentiated picture is necessary. Depending on the required current range and thus the application, different types of Co oxide electrocatalysts are preferred. Applications requiring low overpotentials/low current densities, such as photoelectrochemical water splitting, will benefit from surface restructuring into a disordered, structurally flexible oxyhydroxide phase, which provides superior activity near the onset of the OER. For operation at higher overpotentials/current densities, as commonly employed in alkaline electrolysis, catalysts that exhibit crystalline, structurally stable $Co_3O_4(111)$ or CoOOH(0001) facets may be better suited, due to their smaller Tafel slopes.

Our studies further indicate that the lability toward surface restructuring depends on the Co_3O_4 surface defect structure. Consequently, different applications may require different catalyst preparation procedures that result in optimized surface morphologies, exhibiting either nearly defect-free low-index facets or high densities of defects that enable the structural transformation. Whether such surface engineering of (electro-)catalysts is feasible has been recently challenged, based on the idea that the active catalysts' state is purely determined by the reaction conditions, and every "precatalyst" will thus converge to the same state.[36] In our case, both the defect-free stable state and the defective, restructuring state of our model catalyst surfaces are stable over at least several days under OER conditions at technologically significant current densities. Whether this holds true also over the much longer time scales required for applications is an open question that remains to be clarified. Nevertheless, our work paves the way toward such long-term studies of structurally well-defined model catalysts under more realistic conditions.

The insights obtained here for Co_3O_4, one of the best-studied systems exhibiting surface restructuring, are most likely also relevant for other oxide OER electrocatalysts, for which the occurrence of surface structural transformations and its influence on the catalyst's activity is still often unclear. Further correlative studies of structurally defined electrodes with correlative *operando* structural probes and in-depth electrochemical studies over a wide range of reaction rates are required for a comprehensive understanding of these complex interface phenomena.

ASSOCIATED CONTENT

Data Availability Statement

All XRD, XAS, AFM, and CV data are available at https://crc247.mdi.ruhr-uni-bochum.de/rubric/area-b_b10n_publication_acs_catalysis_2026. EIS data, fitting results, and correlation matrices are available at https://crc247.mdi.ruhr-uni-bochum.de/rubric/area-a_a09n_publications_2025_co3o4_eis-sxrd.

Supporting Information

The Supporting Information is available free of charge at https://pubs.acs.org/doi/10.1021/acscatal.5c08785.

Additional experimental details and figures, including structural characterization, electrochemical studies, *operando* SXRD studies, estimation of the average skin layer thickness, EIS measurements, EIS modeling , and EIS fitting results (PDF)

AUTHOR INFORMATION

Corresponding Authors

Julia Linnemann − *Professur für Technische Elektrochemie, Universität Paderborn, 33098 Paderborn, Germany; Nachwuchsgruppe Gestaltabhängige Elektrochemie, Lehrstuhl für Analytische Chemie, Ruhr-Universität Bochum, 44801 Bochum, Germany;* orcid.org/0000-0001-6883-5424; Email: julia.linnemann@uni-paderborn.de

Fouad Maroun − *Laboratoire de Physique de la Matière Condensée (PMC), CNRS, Ecole Polytechnique, Institut Polytechnique de Paris, F-91120 Palaiseau, France;* orcid.org/0000-0002-5852-2907; Email: fouad.maroun@polytechnique.edu

Olaf M. Magnussen − *Institut für Experimentelle und Angewandte Physik, Christian-Albrechts-Universität zu Kiel, 24098 Kiel, Germany;* orcid.org/0000-0003-4900-0880; Email: magnussen@email.uni-kiel.de

Authors

Carl Hendric Scharf − *Institut für Experimentelle und Angewandte Physik, Christian-Albrechts-Universität zu Kiel, 24098 Kiel, Germany;* orcid.org/0009-0001-3921-3658
Alex Chandraraj − *Institut für Experimentelle und Angewandte Physik, Christian-Albrechts-Universität zu Kiel, 24098 Kiel, Germany*
Konrad Dyk − *Institut für Experimentelle und Angewandte Physik, Christian-Albrechts-Universität zu Kiel, 24098 Kiel, Germany*
Felix Stebner − *Institut für Experimentelle und Angewandte Physik, Christian-Albrechts-Universität zu Kiel, 24098 Kiel, Germany*
Sören Lepin − *Institut für Experimentelle und Angewandte Physik, Christian-Albrechts-Universität zu Kiel, 24098 Kiel, Germany*
Jing Tian − *Institut für Experimentelle und Angewandte Physik, Christian-Albrechts-Universität zu Kiel, 24098 Kiel, Germany*
Laila El Bergmi Byaz − *Laboratoire de Physique de la Matière Condensée (PMC), CNRS, Ecole Polytechnique, Institut Polytechnique de Paris, F-91120 Palaiseau, France*
Jochim Stettner − *Institut für Experimentelle und Angewandte Physik, Christian-Albrechts-Universität zu Kiel, 24098 Kiel, Germany*
Christian Leppin − *Professur für Technische Elektrochemie, Universität Paderborn, 33098 Paderborn, Germany; Nachwuchsgruppe Gestaltabhängige Elektrochemie, Lehrstuhl für Analytische Chemie, Ruhr-Universität Bochum, 44801 Bochum, Germany*
Anastasiia Kotova − *Professur für Technische Elektrochemie, Universität Paderborn, 33098 Paderborn, Germany; Nachwuchsgruppe Gestaltabhängige Elektrochemie, Lehrstuhl für Analytische Chemie, Ruhr-Universität Bochum, 44801 Bochum, Germany*
Sebastian Reinke − *Professur für Technische Elektrochemie, Universität Paderborn, 33098 Paderborn, Germany; Nachwuchsgruppe Gestaltabhängige Elektrochemie, Lehrstuhl für Analytische Chemie, Ruhr-Universität Bochum, 44801 Bochum, Germany*

Complete contact information is available at:
https://pubs.acs.org/10.1021/acscatal.5c08785

Notes

The authors declare no competing financial interest.

ACKNOWLEDGMENTS

We gratefully acknowledge financial support from the Deutsche Forschungsgemeinschaft (DFG) through the Collaborative Research Center SFB/TRR 247 (project number 388390466) and from the Bundesministerium für Forschung, Technologie und Raumfahrt (BMFTR) through the GalvaNection project (project number 03XP0589). S.R. gratefully received support through a scholarship (reference number 20022/051) from the Deutsche Bundesstiftung Umwelt (DBU). We acknowledge DESY (Hamburg, Germany), a member of the Helmholtz Association HGF, for the provision of experimental facilities. Parts of this research were carried out at PETRA III beamline P23, and we would like to thank D. Novikov and A. Khadiev for assistance in using the beamline during the experiment. Beamtime was allocated for proposals I-20220824 and I-20230748. We acknowledge SOLEIL for providing synchrotron radiation facilities, and we would like to thank D. Thiaudière and the beamline staff for assistance in using beamline DiffAbs under proposal 20250286.

REFERENCES

(1) Lewis, N. S.; Nocera, D. G. Powering the planet: Chemical challenges in solar energy utilization. *Proc. Natl. Acad. Sci. U.S.A.* **2006**, *103*, 15729−15735.

(2) Suen, N.-T.; Hung, S.-F.; Quan, Q.; Zhang, N.; Xu, Y.-J.; Chen, H. M. Electrocatalysis for the oxygen evolution reaction: recent development and future perspectives. *Chem. Soc. Rev.* **2017**, *46*, 337−365.

(3) Song, F.; Bai, L.; Moysiadou, A.; Lee, S.; Hu, C.; Liardet, L.; Hu, X. Transition Metal Oxides as Electrocatalysts for the Oxygen Evolution Reaction in Alkaline Solutions: An Application-Inspired Renaissance. *J. Am. Chem. Soc.* **2018**, *140*, 7748−7759.

(4) Burke, M. S.; Enman, L. J.; Batchellor, A. S.; Zou, S.; Boettcher, S. W. Oxygen Evolution Reaction Electrocatalysis on Transition Metal Oxides and (Oxy)hydroxides: Activity Trends and Design Principles. *Chem. Mater.* **2015**, *27*, 7549−7558.

(5) Burke, M. S.; Kast, M. G.; Trotochaud, L.; Smith, A. M.; Boettcher, S. W. Cobalt-Iron (Oxy)hydroxide Oxygen Evolution Electrocatalysts: The Role of Structure and Composition on Activity, Stability, and Mechanism. *J. Am. Chem. Soc.* **2015**, *137*, 3638−3648.

(6) McCrory, C. C. L.; Jung, S.; Ferrer, I. M.; Chatman, S. M.; Peters, J. C.; Jaramillo, T. F. Benchmarking Hydrogen Evolving Reaction and Oxygen Evolving Reaction Electrocatalysts for Solar Water Splitting Devices. *J. Am. Chem. Soc.* **2015**, *137*, 4347−4357.

(7) Bergmann, A.; Martinez-Moreno, E.; Teschner, D.; Chernev, P.; Gliech, M.; de Araújo, J. F.; Reier, T.; Dau, H.; Strasser, P. Reversible amorphization and the catalytically active state of crystalline Co_3O_4 during oxygen evolution. *Nat. Commun.* **2015**, *6*, 8625.

(8) Bergmann, A.; Jones, T. E.; Martinez Moreno, E.; Teschner, D.; Chernev, P.; Gliech, M.; Reier, T.; Dau, H.; Strasser, P. Unified structural motifs of the catalytically active state of Co(oxyhydr)oxides during the electrochemical oxygen evolution reaction. *Nat. Catal.* **2018**, *1*, 711−719.

(9) Tung, C.-W.; Hsu, Y.-Y.; Shen, Y.-P.; Zheng, Y.; Chan, T.-S.; Sheu, H.-S.; Cheng, Y.-C.; Chen, H. M. Reversible adapting layer produces robust single-crystal electrocatalyst for oxygen evolution. *Nat. Commun.* **2015**, *6*, 8106.

(10) Reikowski, F.; Maroun, F.; Pacheco, I.; Wiegmann, T.; Allongue, P.; Stettner, J.; Magnussen, O. M. Operando Surface X-ray Diffraction Studies of Structurally Defined Co_3O_4 and CoOOH Thin Films during Oxygen Evolution. *ACS Catal.* **2019**, *9*, 3811−3821.

(11) Wiegmann, T.; Pacheco, I.; Reikowski, F.; Stettner, J.; Qiu, C. R.; Bouvier, M.; Bertram, M.; Faisal, F.; Brummel, O.; Libuda, J.; Drnec, J.; Allongue, P.; Maroun, F.; Magnussen, O. M. Operando Identification of the Reversible Skin Layer on Co_3O_4 as a Three-Dimensional Reaction Zone for Oxygen Evolution. *ACS Catal.* **2022**, *12*, 3256−3268.

(12) Bouvier, M.; Bubi, I. P.; Wiegmann, T.; Qiu, C. R.; Allongue, P.; Magnussen, O. M.; Maroun, F. Unraveling the Cobalt Oxidation State at the Surface of Epitaxial Cobalt Oxide Films during the Oxygen Evolution Reaction by X-ray Absorption Spectroscopy/Surface X-ray Diffraction. *ACS Appl. Energy Mater.* **2023**, *6*, 7335−7345.

(13) Qiu, C. R.; Maroun, F.; Bouvier, M.; Pacheco, I.; Allongue, P.; Wiegmann, T.; Scharf, C. H.; de Manuel-Gonzalez, V.; Reikowski, F.; Stettner, J.; Magnussen, O. M. Operando Surface X-ray diffraction studies of epitaxial Co_3O_4 and CoOOH thin films during oxygen evolution: pH dependence. *ChemCatChem* **2024**, *16*, No. e202400988.

(14) Faisal, F.; et al. Electrifying model catalysts for understanding electrocatalytic reactions in liquid electrolytes. *Nat. Mater.* **2018**, *17*, 592−598.

(15) Faisal, F.; Bertram, M.; Stumm, C.; Cherevko, S.; Geiger, S.; Kasian, O.; Lykhach, Y.; Lytken, O.; Mayrhofer, K. J. J.; Brummel, O.; Libuda, J. Atomically Defined Co_3O_4(111) Thin Films Prepared in Ultrahigh Vacuum: Stability under Electrochemical Conditions. *J. Phys. Chem. C* **2018**, *122*, 7236−7248.

(16) Davis, E. M.; Bergmann, A.; Zhan, C.; Kuhlenbeck, H.; Cuenya, B. R. Comparative study of Co_3O_4(111), $CoFe_2O_4$(111), and Fe_3O_4(111) thin film electrocatalysts for the oxygen evolution reaction. *Nat. Commun.* **2023**, *14*, 4791.

(17) Davis, E. M.; Bergmann, A.; Kuhlenbeck, H.; Roldan Cuenya, B. Facet dependence of the oxygen evolution reaction on CoO, CoFeO, and FeO epitaxial film electrocatalysts. *J. Am. Chem. Soc.* **2024**, *146*, 13770−13782.

(18) Mefford, J. T.; Akbashev, A. R.; Kang, M. K.; Bentley, C. L.; Gent, W. E.; Deng, H. T. D.; Alsem, D. H.; Yu, Y. S.; Salmon, N. J.; Shapiro, D. A.; Unwin, P. R.; Chueh, W. C. Correlative operando microscopy of oxygen evolution electrocatalysts. *Nature* **2021**, *593*, 67−73.

(19) Luan, C. L.; Corva, M.; Hagemann, U.; Wang, H. C.; Heidelmann, M.; Tschulik, K.; Li, T. Atomic-Scale Insights into Morphological, Structural, and Compositional Evolution of CoOOH during Oxygen Evolution Reaction. *ACS Catal.* **2023**, *13*, 1400−1411.

(20) Wang, C.; Deng, R.; Guo, M.; Zhang, Q. Recent progress of advanced Co_3O_4-based materials for electrocatalytic oxygen evolution reaction in acid: from rational screening to efficient design. *Int. J. Hydrogen Energy* **2023**, *48*, 31920−31942.

(21) Liu, Z. B.; Amin, H. M. A.; Peng, Y. M.; Corva, M.; Pentcheva, R.; Tschulik, K. Facet-Dependent Intrinsic Activity of Single Co_3O_4 Nanoparticles for Oxygen Evolution Reaction. *Adv. Funct. Mater.* **2023**, *33*, 2210945.

(22) Appandairajan, N. K.; Gopalakrishnan, J. A Study of $Co_{3-x}Ni_xO_4$ $(0 \leq x \leq 1)$ system. *Proc. Natl. Acad. Sci., India, Sect. A* **1978**, *87*, 115−120.

(23) Invernizzi, R.; Guerlou-Demourgues, L.; Weill, F.; Lemoine, A.; Dourges, M.-A.; Baraille, I.; Flahaut, D.; Olchowka, J. Controlled Nanostructuration of Cobalt Oxyhydroxide Electrode Material for Hybrid Supercapacitors. *Materials* **2021**, *14*, 2325.

(24) Leppin, C.; Placke-Yan, C.; Bendt, G.; Hernandez, S.; Tschulik, K.; Schulz, S.; Linnemann, J. Interfacial Softening and Electrolyte Uptake in Co_3O_4 OER Catalysts: Insight from Operando Spectroscopy and Fast EQCM-D. *ChemCatChem* **2026**, *18*, No. e01104.

(25) Chen, J.; Wu, X. F.; Selloni, A. Electronic structure and bonding properties of cobalt oxide in the spinel structure. *Phys. Rev. B:Condens. Matter Mater. Phys.* **2011**, *83*, 245204.

(26) Garcia-Mota, M.; Bajdich, M.; Viswanathan, V.; Vojvodic, A.; Bell, A. T.; Noerskov, J. K. Importance of Correlation in Determining Electrocatalytic Oxygen Evolution Activity on Cobalt Oxides. *J. Phys. Chem. C* **2012**, *116*, 21077−21082.

(27) Zasada, F.; Piskorz, W.; Cristol, S.; Paul, J. F.; Kotarba, A.; Sojka, Z. Periodic Density Functional Theory and Atomistic Thermodynamic Studies of Cobalt Spinel Nanocrystals in Wet Environment: Molecular Interpretation of Water Adsorption Equilibria. *J. Phys. Chem. C* **2010**, *114*, 22245−22253.

(28) Zasada, F.; Grybos, J.; Piskorz, W.; Sojka, Z. Cobalt Spinel (111) Facets of Various Stoichiometry-DFT+U and Ab Initio Thermodynamic Investigations. *J. Phys. Chem. C* **2018**, *122*, 2866−2879.

(29) Yan, G.; Sautet, P. Surface Structure of Co_3O_4 (111) under Reactive Gas-Phase Environments. *ACS Catal.* **2019**, *9*, 6380−6392.

(30) Kox, T.; Spohr, E.; Kenmoe, S. Impact of Solvation on the Structure and Reactivity of the $Co_3O_4(001)/H_2O$ Interface: Insights From Molecular Dynamics Simulations. *Front. Energy Res.* **2020**, *8*, 604799.

(31) Kox, T.; Omranpoor, A. H.; Kenmoe, S. Structure and Reactivity of $CoFe_2O_4$(001) Surfaces in Contact with a Thin Water Film. *Physchem* **2022**, *2*, 321−333.

(32) Dhaka, K.; Exner, K. S. Degree of span control to determine the impact of different mechanisms and limiting steps: Oxygen evolution reaction over Co_3O_4(001) as a case study. *J. Catal.* **2025**, *443*, 115970.

(33) Bergmann, A.; Roldan Cuenya, B. Operando Insights into Nanoparticle Transformations during Catalysis. *ACS Catal.* **2019**, *9*, 10020−10043.

(34) Gao, L.; Cui, X.; Sewell, C. D.; Li, J.; Lin, Z. Recent advances in activating surface reconstruction for the high-efficiency oxygen evolution reaction. *Chem. Soc. Rev.* **2021**, *50*, 8428−8469.

(35) Linnemann, J.; Kanokkanchana, K.; Tschulik, K. Design Strategies for Electrocatalysts from an Electrochemist's Perspective. *ACS Catal.* **2021**, *11*, 5318−5346.

(36) Schlögl, R. The functional interface in catalysis. *Arkivoc* **2024**, *3*, 202412178.

(37) Koza, J. A.; He, Z.; Miller, A. S.; Switzer, J. A. Electrodeposition of Crystalline Co_3O_4 - A Catalyst for the Oxygen Evolution Reaction. *Chem. Mater.* **2012**, *24*, 3567−3573.

(38) Pacheco, I.; Bouvier, M.; Magnussen, O. M.; Allongue, P.; Maroun, F. Growth of Ultrathin Well-Defined and Crystalline Films of Co_3O_4 and CoOOH by Electrodeposition. *J. Electrochem. Soc.* **2023**, *170*, 012501.

(39) Schiller, C. A.; Richter, F.; Gülzow, E.; Wagner, N. Validation and evaluation of electrochemical impedance spectra of systems with states that change with time. *Phys. Chem. Chem. Phys.* **2001**, *3*, 374−378.

(40) Reinke, S.; Khamitsevich, V.; Röth, O.; Linnemann, J. Assessment of the Physicochemical Meaning of the Ohmic Series Resistance Observed for High Frequencies in Electrochemical Impedance Spectra. In *2023 International Workshop on Impedance Spectroscopy (IWIS)*; IEEE, 2023; pp 45−50.

(41) Liu, Y.-C.; Koza, J. A.; Switzer, J. A. Conversion of electrodeposited $Co(OH)_2$ to CoOOH and Co_3O_4, and comparison of their catalytic activity for the oxygen evolution reaction. *Electrochim. Acta* **2014**, *140*, 359−365.

(42) Tang, C.-W.; Wang, C.-B.; Chien, S.-H. Characterization of cobalt oxides studied by FT-IR, Raman, TPR and TG-MS. *Thermochim. Acta* **2008**, *473*, 68−73.

(43) Boggio, R.; Carugati, A.; Trasatti, S. Electrochemical surface properties of cobalt oxide (Co_3O_4) electrodes. *J. Appl. Electrochem.* **1987**, *17*, 828−840.

(44) Alex, C.; Sarma, S. C.; Peter, S. C.; John, N. S. Competing Effect of Co^{3+} Reducibility and Oxygen-Deficient Defects Toward High Oxygen Evolution Activity in Co_3O_4 Systems in Alkaline Medium. *ACS Appl. Energy Mater.* **2020**, *3*, 5439−5447.

(45) Xiang, W. K.; Yang, N. T.; Li, X. P.; Linnemann, J.; Hagemann, U.; Ruediger, O.; Heidelmann, M.; Falk, T.; Aramini, M.; DeBeer, S.; Muhler, M.; Tschulik, K.; Li, T. 3D atomic-scale imaging of mixed Co-Fe spinel oxide nanoparticles during oxygen evolution reaction. *Nat. Commun.* **2022**, *13*, 179.

(46) Rabe, A.; Jaugstetter, M.; Hiege, F.; Cosanne, N.; Ortega, K. F.; Linnemann, J.; Tschulik, K.; Behrens, M. Tailoring Pore Size and Catalytic Activity in Cobalt Iron Layered Double Hydroxides and Spinels by Microemulsion-Assisted pH-Controlled Co-Precipitation. *ChemSusChem* **2023**, *16*, No. e202202015.

(47) Kampermann, L.; Klein, J.; Wagner, T.; Kotova, A.; Placke-Yan, C.; Yasar, A.; Jacobse, L.; Lasagna, S.; Leppin, C.; Schulz, S.; Linnemann, J.; Bergmann, A.; Cuenya, B. R.; Bacher, G. Operando Analysis of the Pre-OER Activation of Metal-Doped Co_3O_4 Nanoparticle Catalysts. *ACS Catal.* **2025**, *15*, 18391−18403.

(48) Conway, B. E.; Liu, T. C. Behaviour of surface intermediate states in anodic O_2 evolution electrocatalysis at Co_3O_4 on Ni and Ti substrates. *Ber. Bunsenges. Phys. Chem.* **1987**, *91*, 461−469.

(49) Conway, B. E. *Electrochemical Supercapacitors: Scientific Fundamentals and Technological Applications*; Springer: Boston, MA, 1999.

(50) Zasada, F.; Piskorz, W.; Janas, J.; Grybos, J.; Indyka, P.; Sojka, Z. Reactive Oxygen Species on the (100) Facet of Cobalt Spinel Nanocatalyst and their Relevance in $^{16}O_2/^{18}O_2$ Isotopic Exchange, deN_2O, and $deCH_4$ Processes-A Theoretical and Experimental Account. *ACS Catal.* **2015**, *5*, 6879−6892.

(51) Schwarz, M.; Faisal, F.; Mohr, S.; Hohner, C.; Werner, K.; Xu, T.; Skala, T.; Tsud, N.; Prince, K. C.; Matolin, V.; Lykhach, Y.; Libuda, J. Structure-Dependent Dissociation of Water on Cobalt Oxide. *J. Phys. Chem. Lett.* **2018**, *9*, 2763−2769.

(52) Haunold, T.; Anic, K.; Genest, A.; Rameshan, C.; Roiaz, M.; Li, H.; Wicht, T.; Knudsen, J.; Rupprechter, G. Hydroxylation of an ultrathin Co_3O_4(111) film on Ir(100) studied by in situ ambient pressure XPS and DFT. *Surf. Sci.* **2025**, *751*, 122618.